Nanocellulose-derived carbon/g-C3N4 heterojunction with a hybrid electron transfer pathway for highly photocatalytic hydrogen peroxide production

Yiwei Shan, Ying Guo, Yu Wang, Xiran Du, Jun Yu, Hao Luo, Hui Wu,
Bruno Boury, He Xiao, Liulian Huang, et al.

Nanocellulose-derived carbon/g-C₃N₄ heterojunction with a hybrid electron transfer pathway for highly photocatalytic hydrogen peroxide production

Yiwei Shan [a], Ying Guo [a], Yu Wang [a], Xiran Du [a], Jun Yu [a], Hao Luo [a], Hui Wu [a],

Bruno Boury [b,*], He Xiao [a,*], Liulian Huang [a], Lihui Chen [a]

[a] College of Material Engineering, Fujian Agriculture and Forestry University, Fuzhou, 350108,

China

[b] ICGM, University of Montpellier, CNRS, ENSCM, Montpellier, France

Corresponding authors: Bruno Boury (bruno.boury@umontpellier.fr),

He Xiao (xiaohe_river@163.com)

Abstract

Using oxygen reduction for the photocatalytic production of hydrogen peroxide (H_2O_2) has been considered a green and sustainable route. In the present study, to achieve high efficiency, graphitic carbon nitride (g-C_3N_4) was obtained using thermal polymerization from a bi-component precursor and was then assembled with cellulose nanofibers. It was found that a small quantity of cellulose nanofibers that generates carbon fibers upon pyrolysis greatly improves the photocatalytic activity compared with that of g-C_3N_4 alone. The well-defined carbon/g-C_3N_4 heterojunction-type material exhibits as high as 1.10 mmol L^{-1} h^{-1} of photo-production of H_2O_2 under visible light, which is 4.2 times higher than that yielded by pristine g-C_3N_4 from a single precursor. A comprehensive characterization of the photocatalyst enables us to delineate the effect of the carbon nanofiber with respect to porosity, electron–hole separation, band gap regulation, and especially the electron transfer pathway. Our

28 results demonstrate that nanocellulose-derived carbon, when precisely assembled with

29 other functional material such as a photocatalyst, is a promising promoter of their
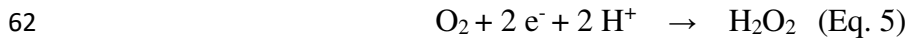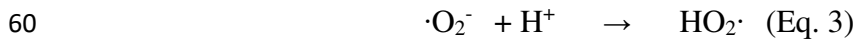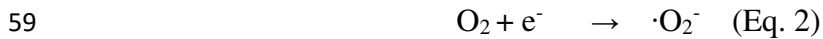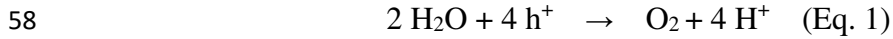
30 activity.

31

34

1. Introduction

36   Hydrogen peroxide (H_2O_2) is a promising energy storage product widely used

37 both as an oxidant and reductant in chemical synthesis, industrial bleaching, and

38 medical sterilization [1, 2]. Moreover, in line with the need for new answers to the

39 increase in energy demand, H_2O_2 has been proposed as the oxidizing agent at the

40 cathode of fuel cells with environmentally acceptable by-products, H_2O and O_2 [3].

41 Presently, the methods adopted to produce H_2O_2 on a large scale are anthraquinone

42 autoxidation [4] and electrochemical synthesis [5]. These methods consume a large

43 amount of energy and organic solvents; in addition, contamination by various organic

44 impurities can occur and result in increased difficulties of purification [6, 7].

45 Consequently, new production processes must succeed in satisfying the demand for

46 H_2O_2, resolve and eliminate the shortcomings of traditional production methods, be

47 efficient, and above all be sustainable and environmentally friendly with respect to the

48 principles of green chemistry.

49   In recent decades, photocatalysis has been employed in light-driven production

50 of H_2O_2 through photoreduction of O_2 in H_2O [8], a process governed by the basic

51 photochemical reaction resulting from light–semiconductor interaction in the presence

52 of water. In this approach, the semiconductor generates holes (h^+) in the valence band

53 (VB) that oxidize H_2O near the surface and release protons (H^+; Eq. 1).

54 Simultaneously, the electrons (e^-) promoted in the conduction band (CB) can reduce

55 O_2 to generate different species, including superoxide radicals ($\cdot O_2^-$) and, subsequently,

56 H_2O_2 by either a (i) single-electron indirect reduction and protonation (Eq. 2–4) or (ii)

57 one-step two-electron direct O_2 reduction (Eq. 5).

58 $$2\,H_2O + 4\,h^+ \quad \rightarrow \quad O_2 + 4\,H^+ \quad (Eq.\ 1)$$

59 $$O_2 + e^- \quad \rightarrow \quad \cdot O_2^- \quad (Eq.\ 2)$$

60 $$\cdot O_2^- + H^+ \quad \rightarrow \quad HO_2\cdot \quad (Eq.\ 3)$$

61 $$HO_2\cdot + H^+ + e^- \quad \rightarrow \quad H_2O_2 \quad (Eq.\ 4)$$

62 $$O_2 + 2\,e^- + 2\,H^+ \quad \rightarrow \quad H_2O_2 \quad (Eq.\ 5)$$

63   ZnO [9] and TiO_2 [10-14] are the two major classical inorganic semiconductors

64 used as photocatalysts [15, 16], among many others. Recently, carbon nitride with

65 graphitic structure (g-C_3N_4) has emerged as a highly promising photocatalyst.

66 Compared with classical metal-based semiconductors, it has a high efficiency and

67 several advantages [17-20], the most attractive one being the absence of metal species

68 known to decompose H_2O_2 via MOOH formation. Additionally, g-C_3N_4-based

69 catalysts exhibit good photostability and photocatalytic activity under visible light.

70 Finally, g-C_3N_4 can be prepared by the polycondensation and pyrolysis (500–600°C)

71 of nitrogen- and carbon-containing precursors such as melamine and urea, both being

72 cheap, abundant, and non-toxic in comparison with ZnO and TiO_2 [21]. However,

73 pure carbon nitride has some bottlenecks limiting its photocatalytic efficiency, such as

74 a fast electron–hole recombination of photogenerated species, insufficient absorption

75 in visible light, a relatively large band gap (~2.7 eV), and a low specific surface area

76 that limits the number of active sites for interfacial photoreactions. To address these

77 issues, different strategies have been employed to enhance the photocatalytic activity,

78 including non-metal doping (e.g., O [22, 23], P [24], N [25], and S [26]), metal ion

79 doping (K [7], Cu [27]), forming heterojunctions with other semiconductors (e.g.,

80 ZnO [28], MnO_2 [29], and CeO_2 [30]), composites with metal nanoparticles (e.g., Au

81 [20] and Ag [31]), and composites with carbonaceous materials (e.g., carbon dots [32],

82 graphene [33], and carbon nanotubes [34]). The carbonaceous materials are selected

83 as an electron transfer agent and photosensitizer in the photocatalysis field to reduce

84 the electron–hole (e^-/h^+) recombination and to increase the absorption of incident light,

85 respectively. Nowadays, the production of such functional carbon should avoid the

86 use of non-renewable and fossil fuel-derived carbon precursors (e.g., polyacrylonitrile

87 [PAN]), and instead use biosourced carbon. Cellulose nanofibers (CNF) are one

88   example, with 1–3 µm length and 5–10 nm width. They not only have the advantage

89   of size but also possess adequate surface functional groups such as -OH and -COOH,

90   facilitating regulation of the growth and chemical anchoring of chemical species such

91   as precursors of inorganic photocatalysts [35]. Therefore, anchoring graphitic-like

92   materials should be possible if they possess compatible functional groups. This

93   implies the necessity of edge functional groups in g-C_3N_4 that possess H-bonding

94   donor or acceptor ability.

95   Various research groups have already demonstrated the synergy of

96   nanocellulose/g-C_3N_4 composites, with or without pyrolysis of the cellulose. It has led

97   to the development of adsorbents or photocatalysts for the oxidation of dyes

98   (methylene blue [36-39] or rhodamine [40, 41]), formaldehyde [42], Cr(IV) [43, 44],

99   oil/water emulsion [45] or bacteria [46] and also the preparation of thermal insulator

100   materials [47, 48]. These are promising routes especially for pollutant remediation;

101   however, the future of photocatalysis also involves the production of chemicals by

102   clean and low-energy processes. To the best of our knowledge, only one previous

103   study used g-C_3N_4 and nanocellulose to produce an efficient photocatalyst to produce

104   chemicals, H_2 in that case. However, nanocellulose was used only as a template to

105   generate a chiral nematic structure in addition to the use of silica, with nanocellulose

106   subsequently eliminated by calcination [49]. In our study, we used nanocellulose as

107   both a template and a C-precursor to prepare a C/g-C_3N_4 composite by the simplest

108   possible process. It is also worth mentioning the work by Jin et al., who used soluble

109   cellulose acetate in combination with melamine as a g-C_3N_4 precursor to produce a

110   C/g-C_3N_4 photocatalyst for the production of hydrogen [50].

111   In the present study, g-C_3N_4 nanosheets (CN2) were fabricated for the first time

112   using a mixture of melamine and urea and a two-step calcination method, to generate

113   a higher proportion of amino groups (-NH_x) than that in g-C_3N_4 prepared with only

114   melamine (CN1); see Scheme 1 for the summary of the general strategy. We found

115   that the as-prepared g-C_3N_4 nanosheets can easily and strongly bind the CNF, possibly

116   by hydrogen or even covalent bonds. The cellulose nanofiber/g-C_3N_4 composite is

117   then transformed by pyrolysis into a covalent heterojunction C/g-C_3N_4 (CNCF1 or

118   CNCF2) with consequences on the band structure and electron transfer process and an

119   important improvement in the photocatalytic activity. As usual when designing a

120   nanocomposite, apart from the nature of the interaction between the components, their

121   mass ratio is an important factor. Prior experiments demonstrated that the optimum

122   mass ratio of the cellulose nanofiber/g-C_3N_4 is ~3–4 %; therefore, this ratio was

123   implemented throughout this study.

124

125   **2. Experimental**

126   *2.1 Materials and reagents*

127   Melamine ($C_3H_6N_6$; 99%), urea (CH_4N_2O; 99.5%), potassium dihydrogen

128   phosphate (KH_2PO_4; 99.5%), potassium hydrogen phosphate (K_2HPO_4; 99%),

129   N,N-Diethyl-p-phenylenediamine sulfate (DPD; 98%), horseradish peroxidase (POD;

130   enzymatic activity >160 units/mg), anhydrous ethanol (AR), 5,5-dimethyl-1-pyrroline

131   N-oxide (DMPO, 97%) were obtained from Aladdin Industrial Co., Ltd, China.

132   Cellulose nanofibers (1 wt% aqueous solution; average length: 1–3 um, average width:

133   5–10 nm) was purchased from Guilin Qihong Technology Co., Ltd., China.

134   Polyethersulfone (PES) membrane ($\varnothing$ 13 mm × 0.22 µm) was obtained from Jin Teng

135   Experimental Equipment Co., Ltd., Tianjin, China. All the chemical reagents

136   mentioned above were of analytical grade and were utilized without further

137   purification.

138
139   *2.2 Preparation of photocatalysts*

140   The g-C_3N_4 nanosheets were synthesized by a two-step pyrolysis treatment of

141   melamine and urea [51]. First, melamine (3.2 g) and urea (0.8 g) were uniformly

142   mixed and thoroughly ground in an agate mortar. The samples were placed into a

143   muffle furnace and heated to 500°C with a heating rate of 2°C min^{-1} in static air and

144   left for 2 h; then, the temperature was risen to 520°C for 2 h at the heating rate of 2°C

145   min^{-1}. The residual yellow solids were ground into powder and calcined at 520°C for

146   4.5 h in air. Finally, the resultant light-yellow products with a productivity of 30%

147   were denoted as CN2. For comparison, g-C_3N_4 nanosheets from a single precursor

148 was also synthesized by calcining pure melamine through the same thermal treatment

149 and denoted as CN1, with a productivity of 36%.

150   The g-C$_3$N$_4$ composited with nanocarbon fibers was prepared by a one-step

151 thermal treatment of the compound of g-C$_3$N$_4$ and CNF. In brief, g-C$_3$N$_4$ nanosheets

152 (CN1 or CN2; 0.10 g) was added into 10 mL of deionized water containing a

153 suspension of CNF (0.33 g; CNF concentration 1 wt%) and ultrasonicated for 30 min,

154 as shown in Figure S1. Subsequently, the mixtures were vacuum-dried at 60°C for 12

155 h. Then, the residual white yellow solids were directly pyrolyzed at 500°C for 1 h at

156 the heating rate of 5°C min^{-1} in argon atmosphere, marked as CNCFx (x = 1, 2). The

157 final products (CNCF1 and CNCF2) obtained also retained the productivity of 80%

158 and 70%, respectively. The pure CNF were carbonized into cellulosic carbon fibers,

159 denoted as CF, under the same calcination conditions.

160

161 *2.3 Characterization*

162   The crystal structures of as-prepared samples were characterized using an X-ray

163 diffractometer (Rigaku, Ultima IV, Japan) with Cu Ka radiation in the range between

164 5° and 80°. Fourier transform infrared (FTIR) spectra were recorded on a Bruker

165 VERTEX 70 spectrophotometer at the wavelength ranging from 400 to 4000 cm^{-1}.

166 The porosimetry measurements and BET-specific surface area of the samples was

167 detected by nitrogen adsorption/desorption on an adsorption apparatus (Micromeritics,

168 ASAP 2020, USA). The morphologies of the samples were observed using a scanning

169 electron microscope (Hitachi, SU8010, Japan) and transmission electron microscope

170 (JEOL, JEM-2100, Japan). The X-ray photoelectron spectrometer (XPS, ESCALAB

171 250, Thermo Scientific, USA) equipped with Al Kα radiation monochromatic source

172 was used to detect chemical composition and elemental states. The ultraviolet

173 (UV)-vis diffuse reflectance spectra (UV-vis DRS) were obtained using a UV-vis

174 spectrophotometer (Cary 500, Varian, USA) in the range of 300–800 nm with BaSO$_4$

175 as a reflectance standard. Photoluminescence spectra were recorded on a LS55

176 spectrophotometer (Perkin-Elmer, USA) under the excitation wavelength of 365 nm at

177 room temperature. Time-resolved photoluminescence (TRPL) spectra were obtained

178 on a fluorescence spectrophotometer (FLS980, Edinburgh Instruments, UK).

179 Photo-generated ·O$_2^-$ radical species in the photocatalytic process were detected with

180 DMPO as a trapping agent. The absorbance of hydrogen peroxide solution was

181 determined by UV–visible spectrophotometer (US-Vis, Agilent 8453, USA) at the

182 wavelength 551 nm.

183 *2.4 Photoelectrochemical and electrochemical measurement*

184   The transient photocurrent curves and electrochemical impedance spectroscopy

185 were obtained on CHI660-E electrochemical workstation (Chenhua Instrument

186 Company, Shanghai, China) based on a three-electrode cell composed of Pt wire as

187 the counter electrode, Ag/AgCl electrode as the reference electrode, and

188 fluorine-doped tin oxide (FTO) glass (1×1 cm^2) as the working electrode. Na_2SO_4

189 aqueous solution (0.2 mol/L) was used as the electrolyte. Five milligrams of the

190 sample (CNx or CNCFx) was added to 1 mL of Nafion solution (0.5%) under

191 ultrasonication for 30 min, and then deposited onto the FTO glass. The as-prepared

192 working electrode was dried at 80°C for 3 h. The photoelectrochemical measurement

193 was performed under visible light irradiation (Xe arc lamp: 300 W, the distance

194 between the surface of the solution and light filter: 10 cm, filter wavelength: $\lambda > 420$

195 nm). The transient photocurrent was collected with the light on and off. The

196 electrochemical impedance spectroscopy (EIS) was tested at the frequency of 0.01

197 and 10^6 Hz with the alternating current amplitude of 5 mV.

198   Rotating disk electrode (RDE) tests were also taken on a CHI660-E

199 electrochemical workstation with a modulated speed rotator and a glassy carbon disk

200 electrode (working electrode). The Ag/AgCl electrode and Pt wire electrode were

201 used as the reference electrode and counter electrode, respectively. Two milligrams of

202 the photocatalyst was dispersed into 1 mL of Nafion solution (10%) under

203 ultrasonication for 30 min. Then, 10 µL of the suspension was dropped on a glassy

204 carbon electrode with a diameter of 5 mm and air-dried at room temperature as the

205 working electrode. The linear sweep voltammetry (LSV) curves were obtained using a

206 phosphate buffer solution (0.1 mmol/L; pH 7) with O_2-saturated purging at a scanning

207 rate of 10 mV/s and the rotating speed between 0 and 2500 rpm.

208

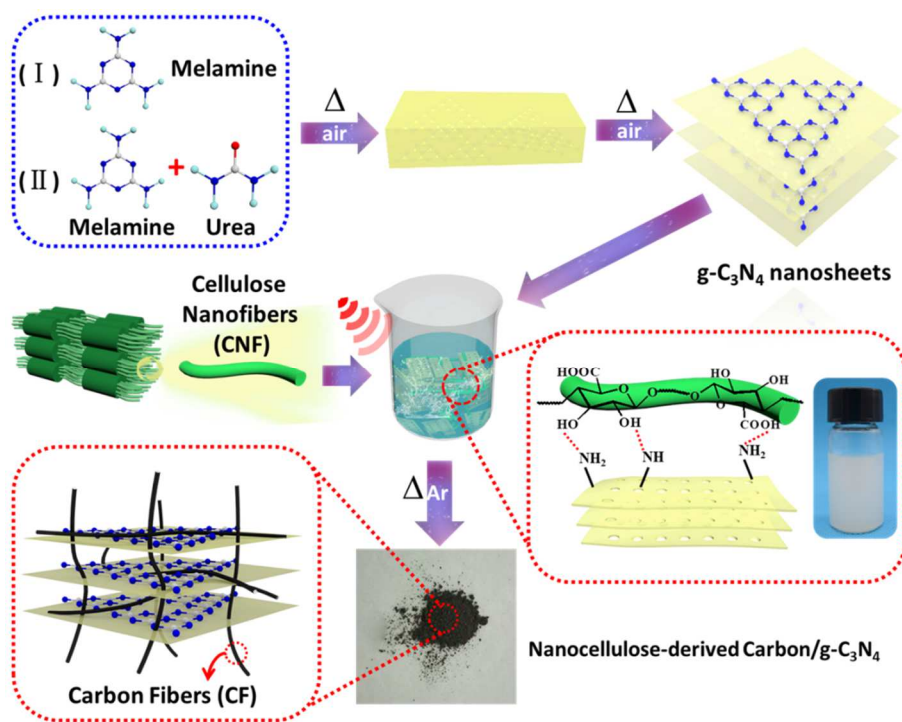209 *2.5 Photocatalytic activity measurements*

210   For evaluating the photocatalytic H_2O_2 generation, the catalyst powder (50 mg)

211 was dispersed in a solution of deionized water (45 mL) and ethanol (5 mL). Then, the

212 suspension was ultrasonicated for 5 min and purged with O_2 gas for 30 min prior to

213 visible irradiation. Then, the photocatalytic performance was examined under visible

light irradiation (Xe arc lamp: 300 W, the distance between surface f the solution and light filter: 10 cm, filter wavelength: $\lambda > 420$ nm) with continuous O_2 purging and stirring for 6 h. Every hour, an aliquot of the suspension (4 mL) was taken and filtered to remove the catalysts. The concentration of H_2O_2 was measured by a colorimetric method. To this end, 5 mL of the filtered solution was immediately mixed with 0.5 mL of phosphate buffer (0.5 M K_2HPO_4 and 0.5 M KH_2PO_4), DPD solution (50 µL), and peroxidase (50 µL), with vigorous shaking for 30 s. Then, the absorbance of the aqueous solution was measured at 551 nm using a UV–visible spectrophotometer [52].

The decomposition behavior of H_2O_2 with photocatalysts was investigated by adding 50 mg of the samples to 50 mL of H_2O_2 solution (1 mmol/L) with continuous stirring under visible light irradiation for 1 h. The stability of the as-prepared samples was evaluated by performing three consecutive tests. When finishing each run, the photocatalyst was collected using membrane filtration and washed with deionized water, then vacuum-dried at 50°C overnight, finally reused in the next cycle under the same conditions. Photocatalytic H_2O_2 concentration was also investigated by measuring the absorbance of the filtrate according to the Beer–Lambert law [52].
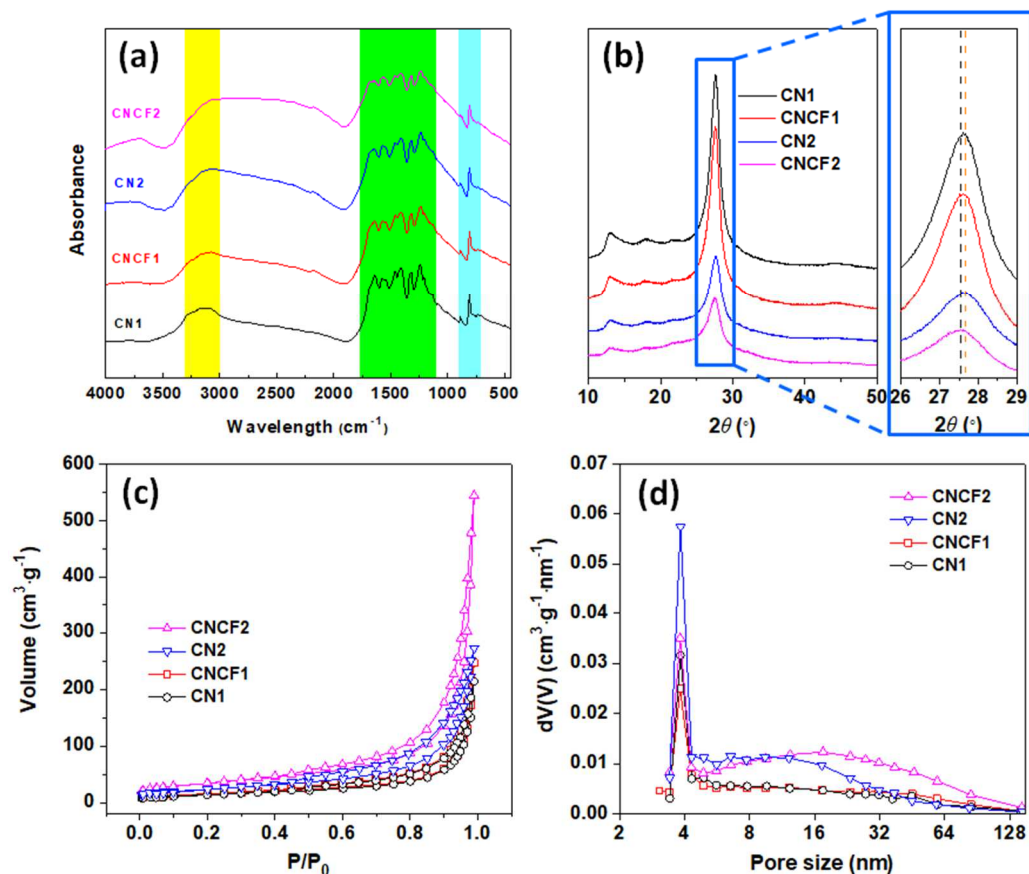

Scheme 1. Procedures for sample synthesis

233

3. Results and discussion

3.1 Photocatalyst preparation and characterization

Specific surface area is important for the activity of a photocatalyst; therefore, a bi-component approach was selected to prepare g-C_3N_4 with the highest possible surface area [53, 54]. Urea was used as an additive to melamine owing to the release of large quantities of volatile gas during thermal treatment, resulting in high porosity [55, 56]. It also can generate a high quantity of residual amino groups, generally on the edges of the nanosheets. Because CNF have surface -OH and -COOH groups, H-bonding and formation of amide or ester groups can occur through reactions with amino-rich carbon nitride. For comparison, a g-C_3N_4 was prepared by the mono-component approach using only melamine, which is referred to as CN1. A comparison between the dispersal behaviors of CN1 and CN2 with CNF in aqueous phase is shown in Figure S1, suggesting a higher stabilization of the suspension in the case of CNF/CN2 mixture.

Carbonization at 500°C of the CNF/CN1 and CNF/CN2 mixtures transforms their CNF into carbon, generating porosity throughout the materials and modifying the hydrophilic/hydrophobic balance of the surface in the corresponding CNCF1 and CNCF2, as shown in Figure S2. The results show that the CN2 (from dual precursors) was more hydrophilic than CN1 (from single precursor) owing to the presence of more hydrophilic groups (amino groups) in CN2. Moreover, the contact angles of CN1 (24.5º) and CN2 (20.5º) respectively decreased to 17.6º (CNCF1) and 11º (CNCF2) when g-C_3N_4 assembled with the carbon nanofibers pyrolyzed from nanocellulose was used, because of the increase in the stacking distance in g-C_3N_4. The optimized mass ratio of CNF/g-C_3N_4 is ~3.3 wt%, which is a miniscule quantity of CNF, but as shown below, it has a substantial effect on the photocatalytic performance compared with pure carbon nitride. Moreover, the sample yield is ~70–80% and with cheap and renewable products. This weight loss is attributed to the decomposition of cellulose and also the condensation reaction between the surface functional groups of cellulose and g-C_3N_4.

Figure 1. Fourier transform infrared spectroscopy curves (a), X-ray diffraction patterns (b), N_2 adsorption-desorption isotherms (c) and pore size distribution derived from desorption isotherm (d) of CN1, CN2, CNCF1, and CNCF2.

The generation of carbon results in an important modification of the color of the material from slightly yellow for pure carbon nitride (CN1 and CN2) to gray for CNCF1 and CNCF2, as shown in Figure S3. Analyzed by FT-IR (Figure 1a), all spectra of CNx and CNCFx (x = 1, 2) are dominated by the signals related to the presence of g-C_3N_4. Several strong bands in the 1200–1600 cm^{-1} region were typical for the stretching modes of the CN heterocycles [57]. The sharp peak at 810 cm^{-1} corresponds to the characteristic breathing vibration of tri-s-triazine units [58]. The broad bands ranging from 3000 cm^{-1} to 3300 cm^{-1} correspond to the NH and OH stretching vibrations [59]. The peak intensity of –NH_x between 3000 cm^{-1} and 3300 cm^{-1} in CNCF1 and CNCF2 is slightly lower than that of CN1 and CN2, respectively; it implies a decrease in the number of amino groups [60].

The presence of g-C$_3$N$_4$ was also clearly detected in the signals observed in the X-ray diffraction powder patterns of the CNx and CNCFx samples, as shown in Figure 1b. The two characteristic peaks at $2\theta = 12.9°$ and $27.5°$ are ascribed to the (100) and (002) diffraction planes of the in-plane repeat tri-s-triazine units and the interlayer stacking reflection of conjugated aromatic segments, respectively [61-63]. A slight downshift in the position of the (002) crystal plane was detected when comparing CN1 and CN2 and CNCFx. It corresponds to a very small increase in the stacking distance in g-C$_3$N$_4$ when assembled with the carbon nanofibers [64], possibly owing to the intercalation of organic species during pyrolysis. A weaker peak intensity of (002) was noted for CN2 and CNCF2 than for CN1 and CNCF1, respectively, which may be ascribed to the effective exfoliation of g-C$_3$N$_4$ into sheet-like structures by overcoming the weak van der Waals forces between layers in the calcination process; this finding is consistent with other reports on g-C$_3$N$_4$ [65].

Porosity of the materials was determined by N$_2$ adsorption-desorption with the isotherms shown in Figure 1c. All samples exhibited typical type IV isotherms with H3 type hysteresis loops, indicating that the samples were micro-, meso-, and slightly macroporous with a specific surface area of 50 m^2 g^{-1} (CN1), 55 m^2 g^{-1} (CNCF1), 83 m^2 g^{-1} (CN2), and 120 m^2 g^{-1} (CNCF2). The data emphasize the effect of CNF in addition to the preparation method of g-C$_3$N$_4$. CN2 and CNCF2 exhibited 1.5–2.4 times higher BET SSA than CN1 and CNCF1 (Table S1). An increase was also observed for the average pore volume, calculated to be 0.34 m^3 g^{-1} (CN1), 0.39 m^3 g^{-1} (CNCF1), 0.44 m^3 g^{-1} (CN2), and 0.85 m^3 g^{-1} (CNCF2; Table S1). Clearly, the bi-component route results in materials with enhanced porosity that is ascribed to a higher proportion of CO$_2$ and NH$_3$ release during calcination [66]. Notably, the assembly of CNF with CN1 or CN2 leads to a decrease in the number of small mesopores and an increase in the number of large mesopores increased, which is expected when considering the formation of carbonaceous residue upon pyrolysis of CNF (Figure 1d).
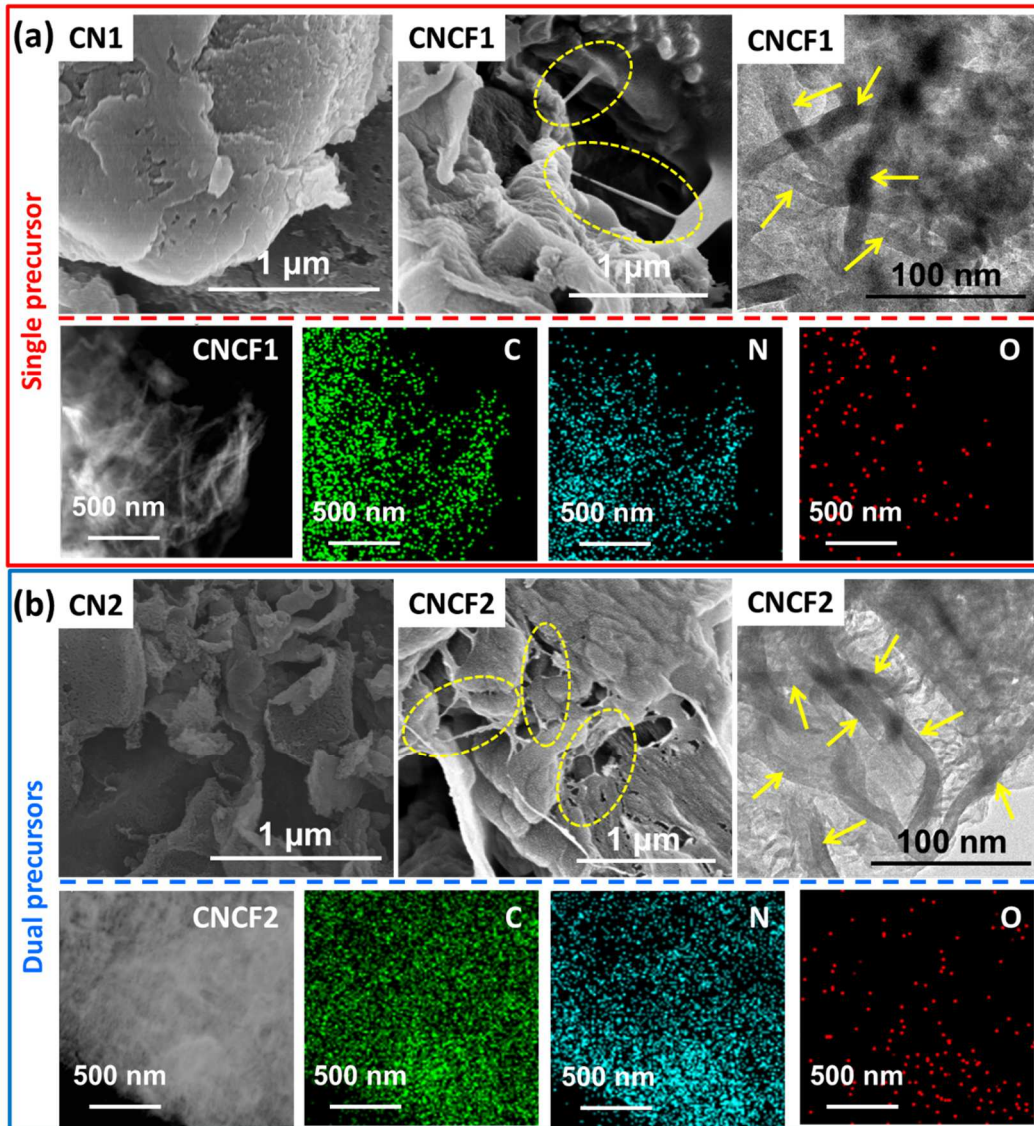
Figure 2. Scanning electron microscopy (SEM) images of CN1 and CNCF1; transmission electron microscopy (TEM) and TEM mapping of CNCF1 (a), SEM images of CN2 and CNCF2; TEM and TEM mapping of CNCF2 (b).

Scanning electron microscopy (SEM) and transmission electron microscopy (TEM) revealed the morphology and microstructure of CNx and CNCFx (x = 1 or 2). As shown in Figure 2, CN1 and CN2 are mainly composed of stacked irregular nanosheets. Compared with CN1, a thinner sheet-like structure was obtained for CN2 upon calcination. For samples after pyrolysis (CNCF1 and CNCF2), carbon nanofibers with an average length of 0.1–1 µm were identified on top of or between micron-sized layers of carbon nitride. Sheet-like carbon nitride particles of 8–12 µm

width were observed by TEM (Figure 2), suggesting that the assembly also occurs at the nanometer scale because isolated carbon nanofibers $\varnothing \approx 10$–20 nm were identified. This clearly showcases the integration of the CNF within the g-C$_3$N$_4$ during the assembly prior to pyrolysis. Elemental mapping by TEM shows that C and N, the two main elements of carbon nitride, are uniformly spread in CNCF1 and CNCF2, and only traces of oxygen are likewise distributed (Figure 2).
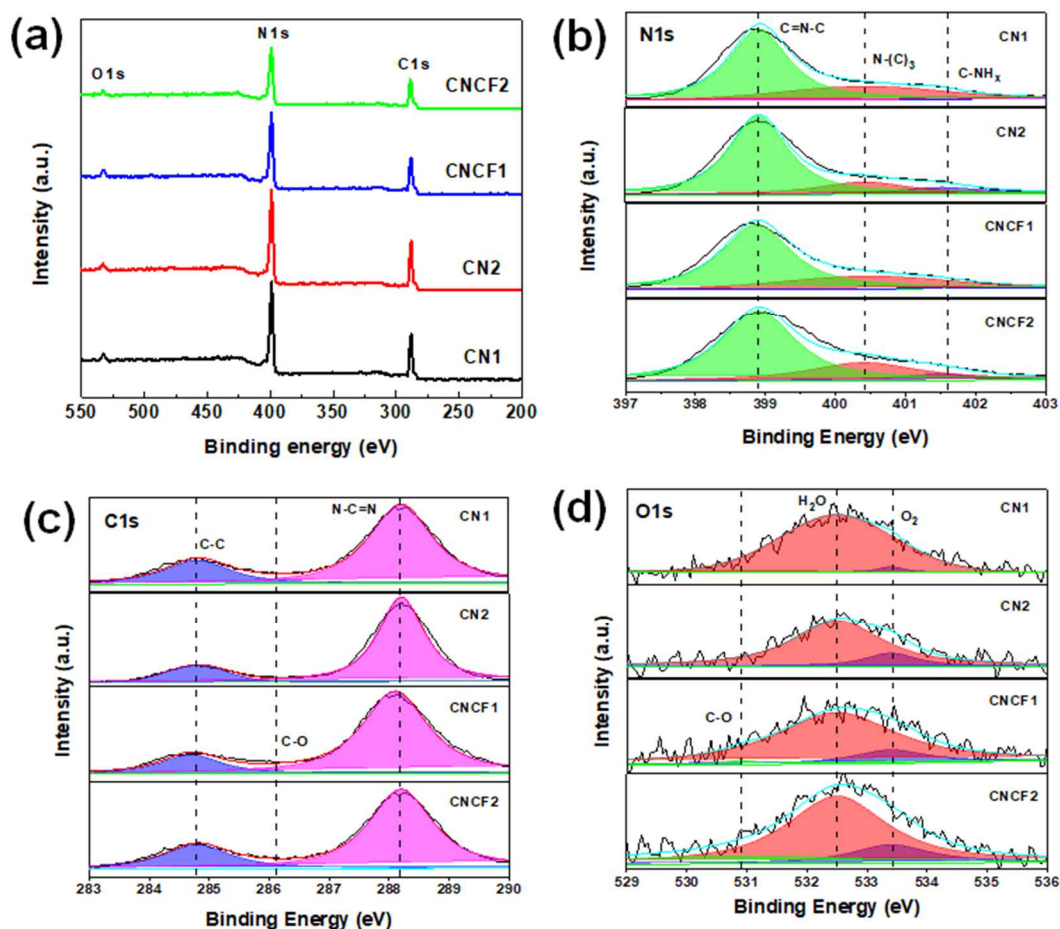
Figure 3. X-ray photoelectron spectroscopy data of CN1, CN2, CNCF1, and CNCF2 samples: survey scan (a), core spectra with deconvolution for N1s (b), C1s (c), and O1s (d).

X-ray photoelectron spectroscopy (XPS) allowed us to identify the composition and chemical status of the main elements in the samples (Figure 3). As shown in Figure 3a, similar X-ray photoelectron spectra were recorded for the four samples exhibiting the two peaks expected for g-C$_3$N$_4$, namely N 1s and C 1s and a weak signal of O 1s [67]. For N 1s spectra in Figure 3b, the three peaks at 398.9, 400.4, and

401.5 eV are assigned to sp^2-hybridized nitrogen (C=N-C), tertiary nitrogen (N-$(C_x)_3$) and C-NH_x, respectively [41]. An estimate of the relative proportion of the different species was obtained by deconvolution (Table S2). It appears that the percentage of C-NH_x either in CN2 or CNCF2 prepared by the bi-component route is considerably higher than that for the materials prepared by the mono-component route (CN1 and CNCF1). This is an additional indication of the effect of the urea precursor during the formation of the materials, and it is consistent with the FT-IR data [68] (Figure 1a). Moreover, the content of C-NH_x decreased after g-C_3N_4 was assembled and pyrolyzed with CNF, a possible explanation being the reaction of this amino group with the functional groups of cellulose (hydroxyl and carboxylic group) during assembly or with gaseous products issued from the decomposition of cellulose during pyrolysis.

In Figure 3c, C 1s spectrum could be deconvoluted into two peaks at 284.8 and 288.2 eV. The peak at 288.2 eV represents by far the highest proportion of C species and was attributed to sp^2-hybridized carbon covalently bound by N atom (N=C-N), as expected for g-C_3N_4. The peak at 284.8 eV was assigned to C-C carbon species [69], both routes of preparation led to a similar quantity of this species, indicating the presence of carbonaceous residue. With the assembly and pyrolysis of CNF, the content of N-C=N decreased by a few percent and that of C-C increased by 10% for CNCF1, which is expected because the pyrolysis of CNF leads to the formation of carbonaceous char that can adsorb on the surface of g-C_3N_4. However, this increase was not observed when comparing CN2 and CNCF2 and is attributable to a higher integration of the carbon fiber into the sheet-like structure of g-C_3N_4. C 1s XPS data also revealed a peak at 286.1 eV for CNCF1 and CNCF2, which was ascribed to C-O [70] that likely results from the assembly and pyrolysis with CNF, which generates O-containing carbon as observed in carbon-derived polysaccharides [71]. However, different routes of preparation resulted in different C-O content: 1–2% in CNCF1 versus 4–5 % for CNCF2. Concerning oxygen, the high-resolution O 1s spectra was fitted based on two reference peaks centered at binding energies of 533.4 eV and 532.5 eV for adsorbed O_2 and adsorbed H_2O, respectively [72]. Compared with the as-prepared g-C_3N_4 samples CN1 and CN2, the new peak at 530.9 eV in

CNF-modified g-C$_3$N$_4$ samples (CNCF1 and CNCF2) was ascribed to C-O [73]. These data are consistent with the C-O content observed on the C1 XPS spectra, the proportion of O in C-O species being 1–2% in CNCF1 and 3–4 % in CNCF2.
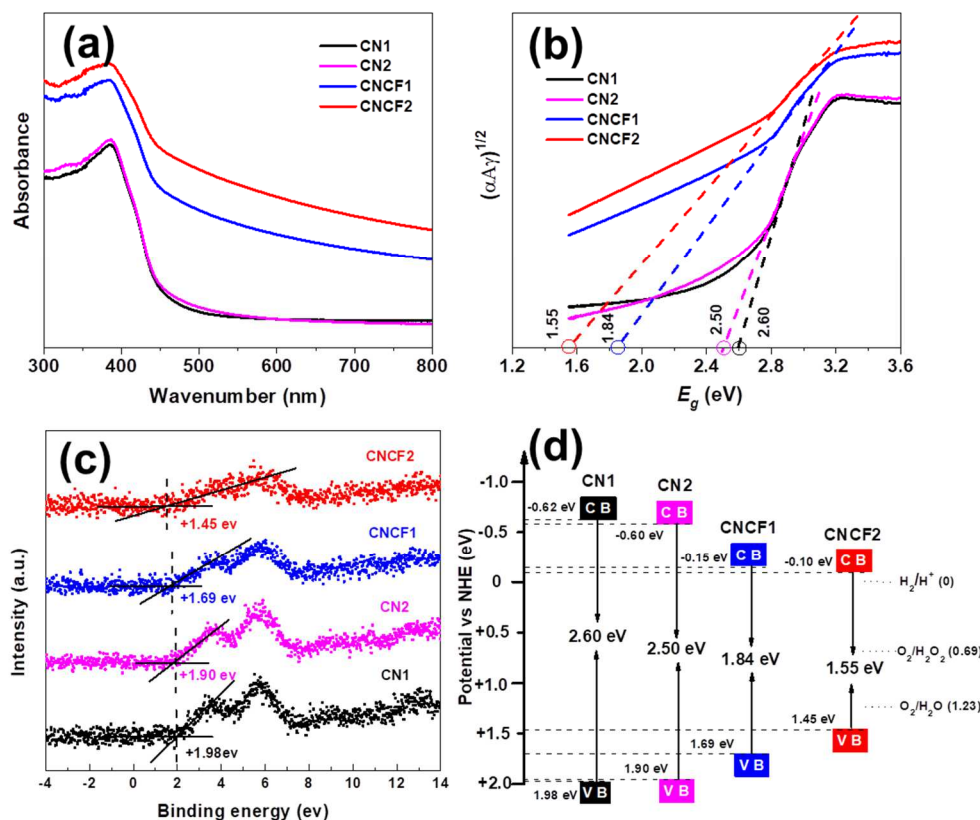
Figure 4. For CN1, CN2, CNCF1, and CNCF2: characterization by UV-vis DRS spectra (a), determination of the band gaps (b), determination of VB XPS spectra (c), and energy band structures (d)

To investigate the optical absorption and band structures, UV–visible diffuse reflectance spectra (UV-vis DRS) of the samples were recorded (Figure 4a). All samples presented absorption in the blue region typical of the 2D structure of carbon nitride [74]. However, compared with CN1 and CN2, the absorption intensity of both CNCF1 and CNCF2 was significantly increased owing to the presence of carbon fibers and multiple reflection of incident ray light across porous structures and band structure regulation [75]. The corresponding band gaps determined from Tauc's plots were 2.60, 2.50, 1.84, and 1.55 eV for CN1, CN2, CNCF1, and CNCF2, respectively

380   (Figure 4b). Therefore, the CNCF1 and CNCF2 samples exhibited a narrower band

381   gap than other samples and consequently higher absorption of visible light useful in

382   photogenerating carriers. The band structures of different samples were further

383   investigated by VB XPS spectra as shown in Figure 4c. An additional effect of the

384   presence of carbon fibers is the variation of the VB potential; values for CN1 (1.98 eV)

385   and CN2 (1.90 eV) were decreased for CNCF1 (1.69 eV) and CNCF2 (1.45 eV). A

386   decrease in the VB potential is beneficial in narrowing the band gap and decreasing

387   the generation of ·OH because of the decreased oxidation ability. Combining the VB

388   XPS spectra (Figure 4c), the location of VB and CB bands was determined using the

389   formula $E_g = E_{VB} - E_{CB}$ (where E_g: band gap, E_{VB}: VB value, E_{CB}: CB value; Figure

390   4d). The E_g of CNCF1 and CNCF2 was smaller than that of CN1 and CN2,

391   respectively. Importantly, the E_g is the smallest for CNCF2, which also has a more

392   positive CB level (-0.1 eV vs NHE) than other samples, which is 0.79 eV more

393   negative than the reduction potential of O_2/H_2O_2 (0.69 eV) and large enough to reduce

394   O_2 to H_2O_2 [76]. Moreover, the positive shift of CB could easily trigger

395   photogenerated electrons from CB, accepting electrons from carbon fibers and

396   enhancing the two-electron reduction of O_2 to H_2O_2 [77, 78].
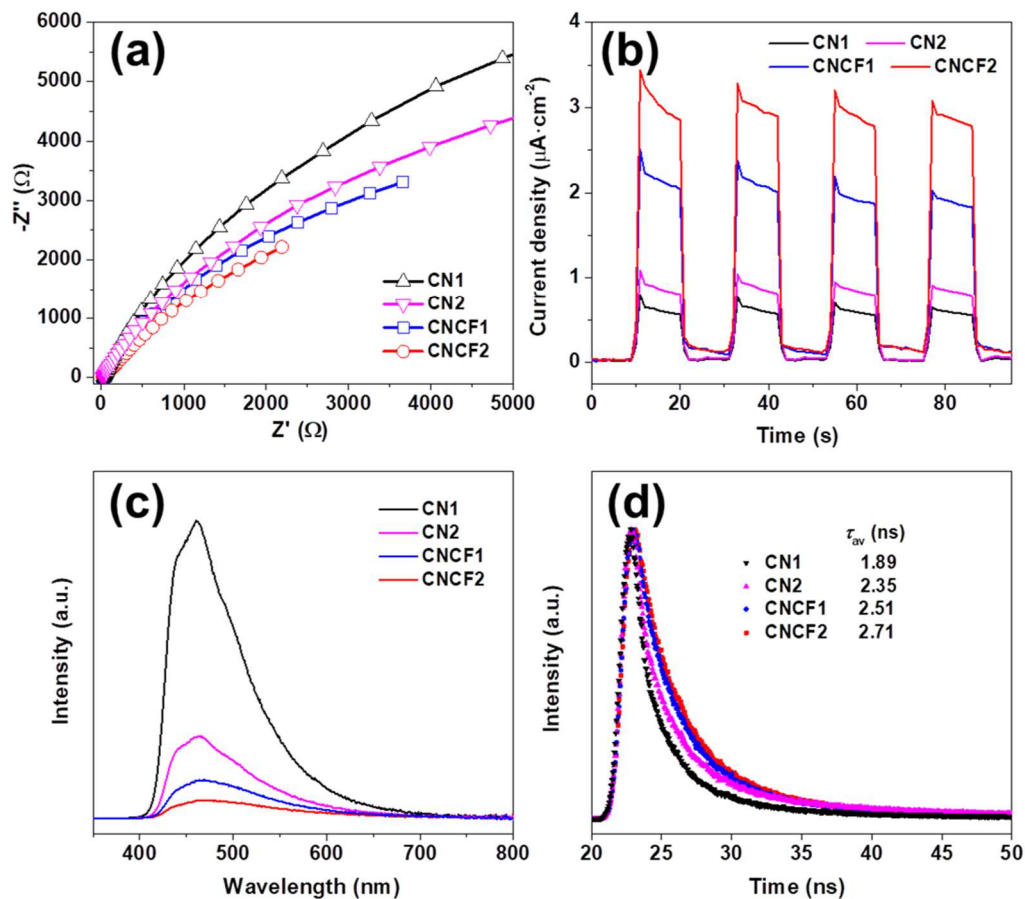
Figure 5. Electrochemical impedance spectra: Nyquist plots (a), transient photocurrent response curves (b), photoluminescence spectra (c), time-resolved photoluminescence decay spectra (d) of the samples.

Electrochemical impedance spectroscopy (EIS) was further employed to understand the charge separation and their transfer. As shown in Figure 5a, the Nyquist plots revealed that under visible light irradiation, the observed arc radius of CNCFx is smaller than the corresponding CNx, which indicates that the charge transfer resistance of CNCFx is significantly decreased. This is ascribed to the introduction of carbon nanofibers and carbonaceous residue that enhance electron transfer. The smaller arc radius of CNCF2 than CNCF1 indicates a faster charge transfer and a better efficiency of electron–hole separation. The transient photocurrent curves under visible light irradiation of the as-prepared samples are shown in Figure 5b. CNCF1 and CNCF2 displayed much higher photocurrent than that of CN1 and CN2, confirming that carbon fibers derived from nanocellulose accelerate electron

413 transfer. The recombination/separation of photogenerated species was investigated by

414 photoluminescence (PL) spectra of the samples (Figure 5c). As a general trend, the

415 lower the photoluminescence peak intensity, the higher the efficiency of

416 photogenerated electron-hole pairs. The strong fluorescence emission peaks of CN1

417 (462 nm) and CN2 (466 nm) were slightly red shifted to 470 nm and 469 nm for

418 CNCF1 and CNCF2, respectively, which further confirms the band gap decrease [79].

419 CNCF1 and CNCF2 samples had considerably lower photoluminescence intensities

420 than CN1 and CN2, respectively, suggesting better separation rate of electrons and

421 holes. Moreover, it is worth noting that the photoluminescence quenching efficiency

422 of CNCF2 was lower than CNCF1, suggesting more effective electron transfer from

423 photogenerated $g\text{-}C_3N_4$ to nanocarbon fibers [74]. To obtain the average radiative

424 lifetime of the recombining charge carriers, time-resolved photoluminescence (TRPL)

425 characterization was investigated (Figure 5d). The average radiative lifetime (τ_{ave}) was

426 further calculated according to the following equation: $\tau_{ave} = (B_1\tau_1^2 + B_2\tau_2^2)/(B_1\tau_1 +$

427 $B_2\tau_2$). The value of τ_{ave} for CN1 and CN2 was 1.89 and 2.35 ns, respectively, whereas

428 that for CNCF1 and CNCF2 was 2.51 and 2.71 ns, respectively. This result indicated

429 that, with the addition of carbon fibers derived from nanocellulose, the markedly

430 extended lifetime of photogenerated charge carriers accelerates the charge separation

431 efficiency. In summary, the presence of cellulose-derived carbon fibers assembled

432 with $g\text{-}C_3N_4$ highly improved the efficiency of the photocatalysts in promoting charge

433 transfer and carrier separation in $g\text{-}C_3N_4$.

434

435

436 **3.2 Photocatalytic production of H_2O_2**
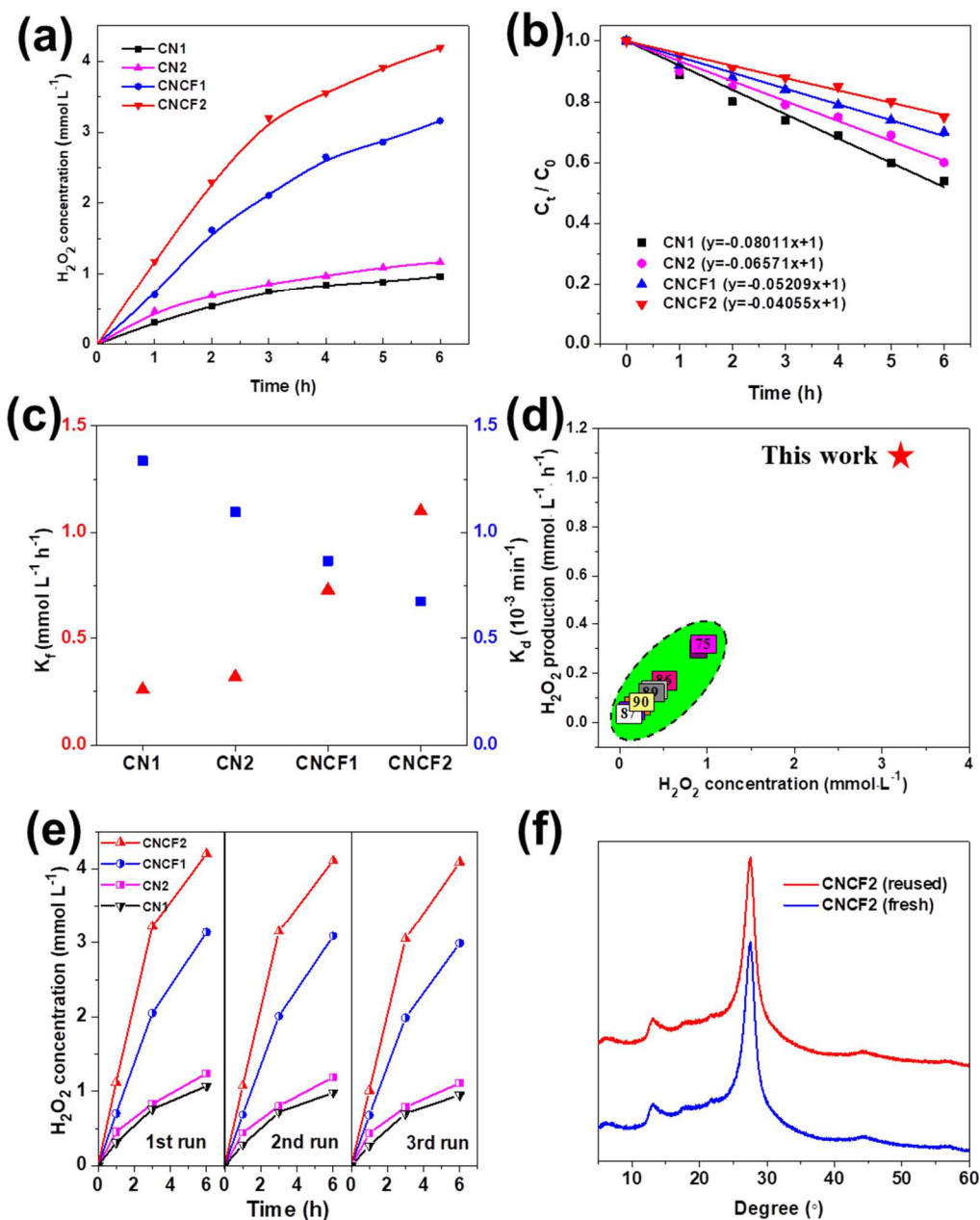
Figure 6. Photocatalytic production of H_2O_2 as a function of time under visible light with CN1, CN2, CNCF1, and CNCF2 as photocatalysts (a); photocatalytic decomposition of H_2O_2 under visible light irradiation (b); formation rate (K_f) and decomposition rate constant (K_d) for H_2O_2 photocatalytic production (c); comparison of reported photocatalytic performances (photocatalytic production rate of H_2O_2 within 3h and H_2O_2 concentration after 3h reaction) (d); reusability assessment of the different photocatalysts (e); X-ray diffraction patterns of CNCF2 before and after photocatalytic H_2O_2 production (f)

446   Photocatalytic production of H_2O_2 under visible light irradiation was evaluated

447   by measuring the quantity of H_2O_2 versus time of reaction under atmospheric pressure

448   at $25 \pm 0.1°C$ using a catalyst concentration of 1.00 ± 0.01 g L^{-1} (Figure 6a). Because

449   ethanol is known to have a good effect on photocatalytic H_2O_2 production when used

450   as a proton donor (Figure S4), 5 mL (85.9 mmol) ethanol was used in this

451   photocatalytic system with an ethanol-to-water ratio of 1: 9 (v/v). With CN1, only

452   0.31 mmol L^{-1} of H_2O_2 is formed after 1 h. Although the productivity is improved

453   with CN2, it remains low: 0.47 mmol L^{-1} of H_2O_2 after 1 h. CNCF1 and CNCF2

454   presented a considerably higher H_2O_2 productivity after 1 h, 0.7 mmol L^{-1} and 1.18

455   mmol L^{-1}, respectively. Therefore, the kinetic study presented in Figure 6c suggests

456   that the order of photocatalytic efficiency is as follows: CNCF2 > CNCF1 > CN2 >

457   CN1.

458   The decomposition behavior of H_2O_2 was investigated under visible light

459   irradiation with photocatalysts and a H_2O_2 concentration =1 mmol L^{-1}. As shown in

460   Figure 6b, the level of H_2O_2 decomposition was ~8% and ~5% with CNCF1 and

461   CNCF2, respectively, after 1 h of visible light irradiation, which was lower than that

462   with CN1 and CN2 (~10%). The H_2O_2 decomposition rate constant (K_d) was

463   calculated with the following equation: $K_d = -\ln(C_t/C_0)/t$, where C_t is the H_2O_2

464   concentration at time t, and C_0 is the initial concentration of H_2O_2 (1 mmol L^{-1}).

465   Figure 6c shows that the K_d of CN1 (1.335×10^{-3} min^{-1}) and CN2 (1.095×10^{-3} min^{-1})

466   was higher than that of CNCF1 (0.868×10^{-3} min^{-1}) and CNCF2 (0.676×10^{-3} min^{-1}).

467   These results confirm that carbon fibers derived from nanocellulose effectively inhibit

468   the decomposition of H_2O_2 on carbon nitride.

469   Compared with previously reported values [7, 75, 80-86], the photocatalyst

470   CNCF2 presented a significantly improved activity (Figure 6d). To investigate the

471   recyclability of the as-prepared photocatalysts, after 6 h of reaction time, the catalyst

472   was separated and washed from the suspension by filtration and then used again in a

473   new batch of H_2O_2 production under the same conditions (Figure 6e). After three

474   cycles, the photocatalyst was almost unchanged and the photocatalytic activity was

maintained. The X-ray diffraction analysis showed that both the fresh and reused
CNCF2 catalysts exhibited almost the same typical peaks, as shown in Figure 6f.
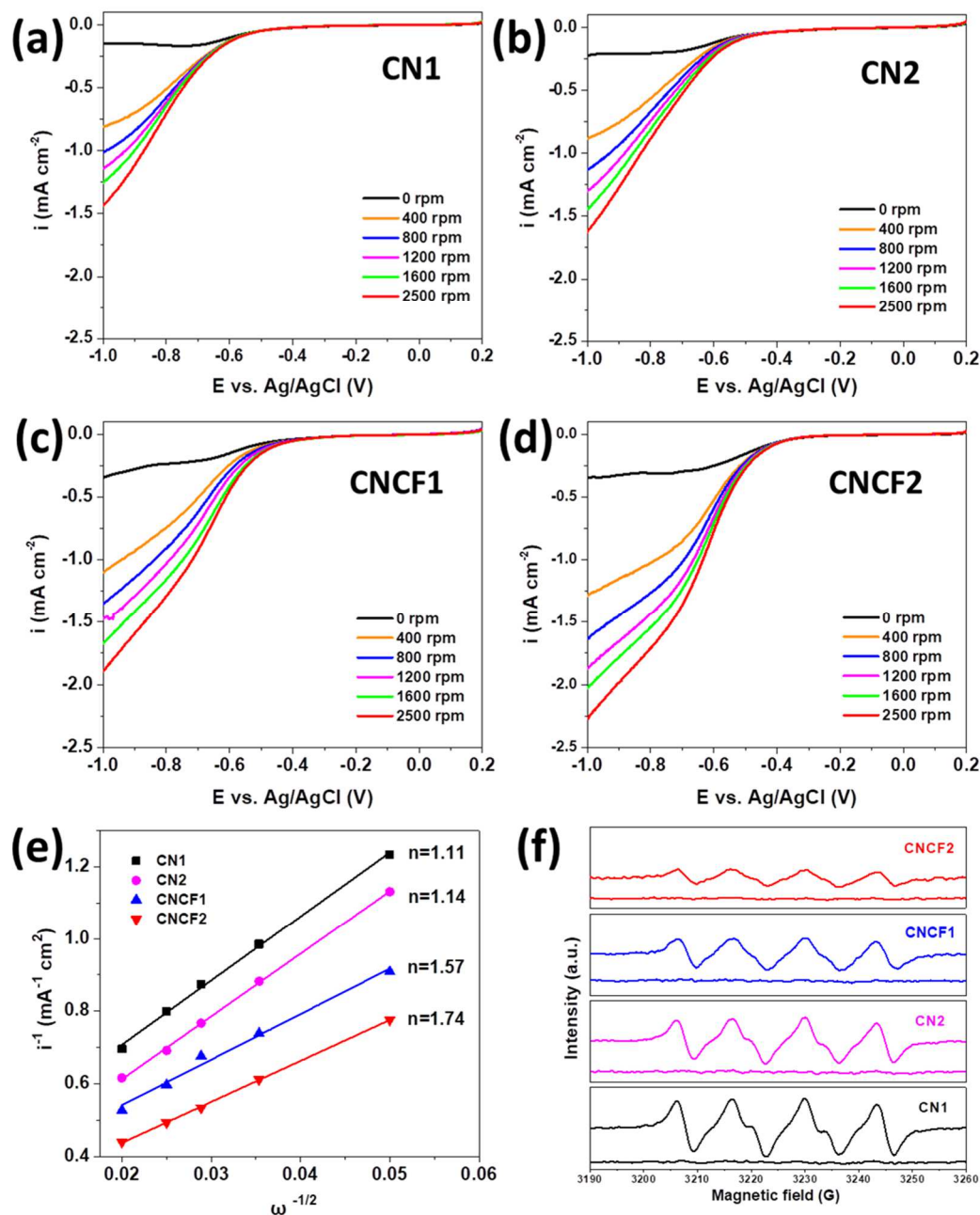
Figure 7. Linear sweep voltammetry curves of CN1 (a), CN2 (b), CNCF1 (c) and CNCF2 (d) measured on a rotating disk electrode at different rotating speeds; Koutecky-Levich plots of the data obtained at a constant electrode potential (-1.0 V vs. Ag/AgCl) (e), Electron paramagnetic resonance spectra of the DMPO-·O_2^- adduct (f)

484   To further investigate the O_2 reduction pathway, a rotating disk electrode (RDE)

485 analysis of the O_2 reduction reaction (ORR) was performed. The linear sweep

486 voltammetry (LSV) curves in Figure 7a-d for the as-prepared samples were measured

487 by an RDE in phosphate buffer solution (0.1 mol L^{-1}, pH = 7) at different rotating

488 speeds. The Koutecky-Levich plots derived from the LSV data are presented in Figure

489 7e. The average number of transfer electrons was calculated using the following

490 equations:

$$j^{-1} = j_k^{-1} + B^{-1}\omega^{-1/2}$$

491

$$B = 0.2nFv^{-1/6}CD^{2/3}$$

492

493 , where j is the current density, j_k is the kinetic current density, ω is the rotating speed,

494 F is the Faraday constant (96485 C mol^{-1}), v is the kinetic viscosity of water (0.01 cm^2

495 s^{-1}), and C is the O_2 concentration in water (1.26 × 10^{-5} cm^2 s^{-1}). The average number

496 of electrons (n) was 1.11 and 1.14 for CN1 and CN2, respectively, and 1.57 and 1.74

497 for CNCF1 and CNCF2, respectively. These results suggest that single-electron O_2

498 reduction occurs on CN1 and CN2 because the n value of CN1 and CN2 was

499 approximately 1. In contrast, the average number of electrons is above 1.5 when

500 nanocellulose-derived carbon is present, especially for CNCF2, for which an O_2

501 reduction by two-electron process is likely. Thus, the ORR for CNCF1 and CNCF2

502 had a hybrid single/two-electron function, whereas that for CN1 and CN2 showed

503 only single-electron function.

504   Electron paramagnetic resonance (EPR) analysis with DMPO as a trapping agent

505 of $\cdot O_2^-$ was performed to identify the pathway of conversion of molecular oxygen to

506 H_2O_2. As shown in Figure 7f, the characteristic peaks of DMPO-$\cdot O_2^-$ were observed in

507 all samples, indicating that $\cdot O_2^-$ was generated as an intermediate in the formation of

508 H_2O_2. As seen in Figure 7f, CN1 and CN2 both presented higher-intensity EPR

509 signals than CNCF1 and CNCF2, indicating that CN1 and CN2 generate more $\cdot O_2^-$

510 than CNCF1 and CNCF2. The finding implies that reduction of O_2 into $\cdot O_2^-$ occurs on

511 the four samples by a single-electron pathway leading to H_2O_2 formation. It is

512 interesting that, CNCF1 and CNCF2 present partial O_2 directly reduction into H_2O_2

513 by a two-electron pathway[87]. Scheme 2 illustrates photocatalytic H_2O_2 production

514 by nanocellulose-derived $C/g-C_3N_4$ nano-heterojunction. Cellulose nanofibers with

515 -OH and -COOH groups can bind to carbon nitride with intrinsic amino groups (-NH,

516 $-NH_2$) and thermally transform into an effective heterojunction, increasing the linking

517 between $g-C_3N_4$ nanosheets and carbon fibers. Furthermore, the carbon fibers reduce

518 the band gap and greatly increase the electron transfer during the photocatalytic

519 reaction. The photocatalytic efficiency also depends on the capacity and strength of

520 adsorption of molecular oxygen onto the surface of carbon nitride. By porosimetrie,

521 BET SSA of CN2 is 2.2 times higher than that of CN1 (Table S1), which provides

522 more space and active sites to adsorb oxygen molecules [88]. The adsorption strength

523 of molecular oxygen is also potentially reinforced by the presence of N atoms of

524 amino groups in CN2, which are able to bind to oxygen as a Lewis acid [89]. As

525 previously reported, such adsorption of oxygen on the surface of the photocatalyst

526 catalyst is highly beneficial to the electron transfer [90]. An exciting point is to

527 observe that with the presence of carbon nanofiber, the EPR intensity of $\cdot O_2^-$ of

528 CNCF1 is higher than CNCF2. The data demonstrate the interest of the bi-component

529 synthetic route chosen for the preparation of the $g-C_3N_4$. This is ascribed to both the

530 larger BET specific surface area and the specific photophysical properties.

531
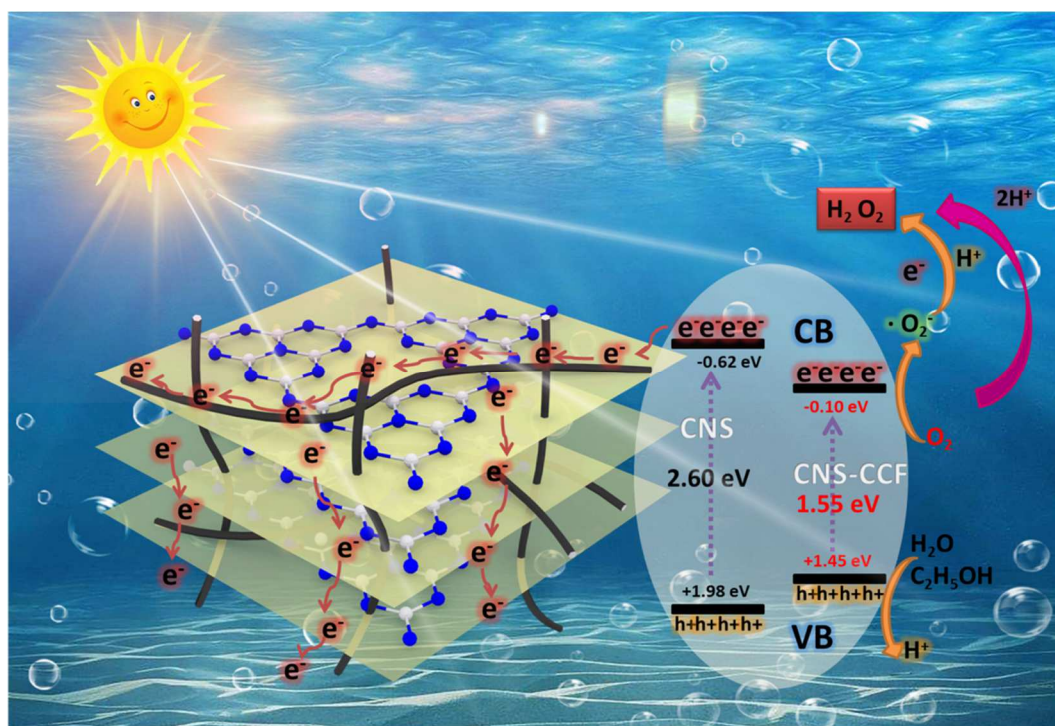
Scheme 2. Role of cellulosic carbon fibers for photocatalytic H_2O_2 production photocatalyzed by a nanocellulose-derived carbon/g-C_3N_4 nanocomposite.

4. Conclusions

The high improvement of the photocatalytic production of hydrogen peroxide (H_2O_2) over carbon nitride (g-C_3N_4) that we report is ascribable of main major phenomenon. First, we show that the presence of a very low content of nanocellulose-derived carbon deeply modify the photoactivity of the g-C_3N_4 assembled with it. The result is an outstanding photocatalytic H_2O_2 production of 1.10 mmol L^{-1} h^{-1} under visible light. The second critical point is to achieve a high level of interaction between the g-C_3N_4 nanosheets and CNF when assembling these two nanocomponents. Third, a high level of interaction can be achieved through the preparation of amino-rich g-C_3N_4 using a bi-component mixture of melamine and urea. When carbon fibers are closely incorporated into the stacked structure of g-C_3N_4, the nanofibers not only improve the porosity of the materials but also have a strong effect on the photophysical properties of the g-C_3N_4 in narrowing the band gap; improving the visible light absorption; increasing the number of photogenerated carriers, especially excitable electrons; and accelerating the electron transfer and further promoting a direct two-electron O_2 reduction reaction to generate hydrogen peroxide. In subsequent studies, this approach will be tested for other materials for the photoproduction of other chemicals.

References

[1] W.C. Hou, Y.S. Wang, ACS Sustainable Chemistry & Engineering 5 (2017) 2994-3001.

[2] H. Hou, X. Zeng, X. Zhang, Angewandte Chemie-International Edition 59 (2019) 17356-17376.

[3] Y. Yang, R.Z. Dong, Y.L. Zhu, H.S. Li, H. Zhang, X.M. Fan, H.L. Chang, Chemical Engineering Journal 381 (2020) 122749.

[4] T. Kato, K. Yoshizawa, European Journal of Organic Chemistry 2011 (2011) 4113-4120.

[5] Y. Sun, L. Silvioli, N.R. Sahraie, W. Ju, J. Li, A. Zitolo, S. Li, A. Bagger, L. Arnarson, X. Wang, T. Moeller, D. Bernsmeier, J. Rossmeisl, F. Jaouen, P. Strasser, Journal of the American Chemical Society 141 (2019) 12372-12381.

[6] H. Hirakawa, S. Shiota, Y. Shiraishi, H. Sakamoto, S. Ichikawa, T. Hirai, ACS Catalysis 6 (2016) 4976-4982.

[7] S. Kim, G.-h. Moon, H. Kim, Y. Mun, P. Zhang, J. Lee, W. Choi, Journal of Catalysis 357 (2018) 51-58.

[8] L. Yang, G. Dong, D.L. Jacobs, Y. Wang, L. Zang, C. Wang, Journal of Catalysis 352 (2017) 274-281.

[9] C. Kormann, D.W. Bahnemann, M.R. Hoffmann, Environmental Science & Technology 22 (1988) 798-806.

[10] D. Tsukamoto, A. Shiro, Y. Shiraishi, Y. Sugano, S. Ichikawa, S. Tanaka, T. Hirai, ACS Catalysis 2 (2012) 599-603.

[11] T. Hirakawa, Y. Nosaka, The Journal of Physical Chemistry C 112 (2008) 15818-15823.

[12] M. Teranishi, S. Naya, H. Tada, Journal of the American Chemical Society 132 (2010) 7850-7851.

[13] H. Goto, Y. Hanada, T. Ohno, M. Matsumura, Journal of Catalysis 225 (2004) 223-229.

[14] L. Zheng, J. Zhang, Y.H. Hu, M. Long, The Journal of Physical Chemistry C 123 (2019) 13693-13701.

[15] S. Sun, X. Yu, Q. Yang, Z. Yang, S. Liang, Nanoscale Advances 1 (2019) 34-63.

[16] C. Ray, T. Pal, Journal of Materials Chemistry A 5 (2017) 9465-9487.

[17] Z. Haider, H.I. Cho, G.H. Moon, H.I. Kim, Catalysis Today 335 (2019) 55-64.

[18] Z. Li, N. Xiong, G. Gu, Dalton Transactions 48 (2019) 182-189.

592   [19] X. Li, J. Zhang, F. Zhou, H. Zhang, J. Bai, Y. Wang, H. Wang, Chinese Journal of Catalysis
593   39 (2018) 1090-1098.

594   [20] G.F. Zuo, S.S. Liu, L. Wang, H. Song, P.X. Zong, W.S. Hou, B.D. Li, Z.L. Guo, X.G. Meng,
595   Y. Du, T. Wang, V.A.L. Roy, Catalysis Communication 123 (2019) 69-72.

596   [21] A. Thomas, A. Fischer, F. Goettmann, M. Antonietti, J.O. Muller, R. Schlogl, J.M. Carlsson,
597   Journal of Materials Chemistry 18 (2008) 4893-4908.

598   [22] S. Samanta, R. Yadav, A. Kumar, A.K. Sinha, R. Srivastava, Applied Catalysis
599   B-Environmental 259 (2019) 118054.

600   [23] H. Wang, Y.H. Guan, S.Z. Hu, Y.B. Pei, W.T. Ma, Z.P. Fan, Nano 14 (2019) 1950023.

601   [24] J. Tian, T.J. Wu, D. Wang, Y. Pei, M.H. Qiao, B.N. Zong, Catalysis Today 330 (2019)
602   171-178.

603   [25] X.Y. Qu, S.Z. Hu, P. Li, Z. Li, H. Wang, H.F. Ma, W. Li, Diamond and Related Materials 86
604   (2018) 159-166.

605   [26] L.H. Zheng, J.Z. Zhang, Y.H. Hu, M.C. Long, Journal of Physical Chemistry C 123 (2019)
606   13693-13701.

607   [27] S.Z. Hu, X.Y. Qu, P. Li, F. Wang, Q. Li, L.J. Song, Y.F. Zhao, X.X. Kang, Chemical
608   Engineering Journal 334 (2018) 410-418.

609   [28] H.L. Tian, H.Q. Fan, J.W. Ma, L.T. Ma, G.Z. Dong, Electrochim Acta 247 (2017) 787-794.

610   [29] Y.J. Zhou, L. Li, Y.H. Wan, T.T. Chen, X. Chu, Analytic Methods 10 (2018) 5084-5090.

611   [30] W. Liu, J.B. Zhou, Z.S. Hu, Separation Purification Technology 227 (2019) 115665.

612   [31] Y.K. Wang, S.Z. Hu, Q. Li, G.Z. Gu, Y.F. Zhao, H.Y. Liang, W. Li, RSC Advances 8 (2018)
613   36903-36909.

614   [32] S. Asadzadeh-Khaneghah, A. Habibi-Yangjeh, K. Nakata, Journal of Photochemistry and
615   Photobiology A-Chemistry 374 (2019) 161-172.

616   [33] D.L. Jiang, Y. Zhang, H.Y. Chu, J. Liu, J. Wan, M. Chen, RSC Advances 4 (2014)
617   16163-16171.

618   [34] S. Zhao, T. Guo, X. Li, T.G. Xu, B. Yang, X. Zhao, Applied Catalysis B-Environmental 224
619   (2018) 725-732.

620   [35] M.L. Foresti, A. Vázquez, B. Boury, Carbohydrate Polymers 157 (2017) 447-467.

621   [36] T. Dou, L. Zang, Y. Zhang, Z. Sun, L. Sun, C. Wang, Materials Letters 244 (2019) 151-154.

622   [37] H. Wang, J. Li, N. Ding, X. Zeng, X. Tang, Y. Sun, T. Lei, L. Lin, Chemical Engineering

623   Journal 386 (2020) 124021.

624   [38] P. Yang, J. Wang, G. Yue, R. Yang, P. Zhao, L. Yang, X. Zhao, D. Astruc, Journal of

625   Photochemistry and Photobiology A: Chemistry 388 (2019) 112169.

626   [39] W. Bai, X. Yang, X. Du, Z. Qian, Y. Zhang, L. Liu, J. Yao, Applied Surface Science 504

627   (2020) 144179.

628   [40] H. Zhao, S. Chen, X. Quan, H. Yu, H. Zhao, Applied Catalysis B: Environmental 194 (2016)

629   134-140.

630   [41] H. Qi, X. Ji, C. Shi, R. Ma, Z. Huang, M. Guo, J. Li, Z. Guo, Journal of Colloid Interface

631   Science 556 (2019) 366-375.

632   [42] X. Li, X. Qian, X. An, J. Huang, Applied Surface Science 487 (2019) 1262-1270.

633   [43] S. Chen, W. Lu, J. Han, H. Zhong, T. Xu, G. Wang, W. Chen, Chemical Engineering Journal

634   359 (2019) 119-129.

635   [44] S. Wang, F. Li, X. Dai, C. Wang, X. Lv, G.I.N. Waterhouse, H. Fan, S. Ai, Journal of

636   Hazardous Materials 384 (2020) 121417.

637   [45] F. Li, Z. Yu, H. Shi, Q. Yang, Q. Chen, Y. Pan, G. Zeng, L. Yan, Chemical Engineering

638   Journal 322 (2017) 33-45.

639   [46] S.-W. Zhao, M. Zheng, H.-L. Sun, S.-J. Li, Q.-J. Pan, Y.-R. Guo, Dalton Transactions (2019)

640   3723-3734.

641   [47] B. Wu, L. Ge, H. Wu, X. Wang, Q. Ge, J. Miao, M. Cao, P. Chen, R. Xia, J. Qian, Advanced

642   Materials Interfaces 6 (2019) 1801406.

643   [48] L. Mu, L. Shi, Y. Wang, Q. Zhou, J. Ye, X. Feng, Journal of Materials Chemistry C 6 (2018)

644   12660-12667.

645   [49] W.S. Lin, W. Hong, L. Sun, D. Yu, D.S. Yu, X.D. Chen, Chemsuschem 11 (2018) 114-119.

646   [50] Z. Jin, J. Chen, S. Huang, J. Wu, Q. Zhang, W. Zhang, Y.-J. Zeng, S. Ruan, T. Ohno,

647   Catalysis Today 315 (2018) 149-154.

648   [51] Y. Li, R. Jin, Y. Xing, J. Li, S. Song, X. Liu, M. Li, R. Jin, Advanced Energy Materials 6

649   (2016) 1601273.

650   [52] L. Liu, W. Sun, W. Yang, Q. Li, J.K. Shang, Scientific Reports 6 (2016) 20878.

651   [53] F. Dong, Z. Zhao, T. Xiong, Z. Ni, W. Zhang, Y. Sun, W.-K. Ho, ACS Applied Materials &

652   Interfaces 5 (2013) 11392-11401.

653   [54] F. Dong, Z. Ni, P. Li, Z. Wu, New Journal of Chemistry 39 (2015) 4737-4744.

654   [55] S. Martha, A. Nashim, K.M. Parida, Journal of Materials Chemistry A 1 (2013) 7816-7824.

655   [56] D.M. Ruan, S. Kim, M. Fujitsuka, T. Majima, Applied Catalysis B-Environmental 238 (2018)

656   638-646.

657   [57] J. Tian, D. Wang, S. Li, Y. Pei, M. Qao, Z.-H. Li, J. Zhang, B. Zong, ACS Sustainable

658   Chemistry & Engineering 8 (2020) 594-603.

659   [58] Y.L. Li, P.P. Li, J.S. Wang, Y.L. Yang, W.Q. Yao, Z. Wei, J.S. Wu, X.X. Yan, X.F. Xu, Y.H.

660   Liu, Y.F. Zhu, Applied Catalysis B-Environmental 225 (2018) 519-529.

661   [59] F. Dong, Z.Y. Wang, Y.J. Sun, W.K. Ho, H.D. Zhang, Journal of Colloid Interface Science

662   401 (2013) 70-79.

663   [60] H. Yu, R. Shi, Y. Zhao, T. Bian, Y. Zhao, C. Zhou, G.I.N. Waterhouse, L.Z. Wu, C.H. Tung, T.

664   Zhang, Advanced Materials 29 (2017) 1605148.

665   [61] A.J. Cai, Q. Wang, Y.F. Chang, X.P. Wang, Journal of Alloys and Compounds 692 (2017)

666   183-189.

667   [62] Y. Yang, C. Zhang, D. Huang, G. Zeng, J. Huang, C. Lai, C. Zhou, W. Wang, H. Guo, W. Xue,

668   R. Deng, M. Cheng, W. Xiong, Applied Catalysis B: Environmental 245 (2019) 87-99.

669   [63] J.S. Zhang, Y. Chen, X.C. Wang, Energy & Environmental Science 8 (2015) 3092-3108.

670   [64] P. Niu, H. Li, Y. Ma, T. Zhai, The Journal of Physical Chemistry C 122 (2018) 20717-20726.

671   [65] J. Xu, L. Zhang, R. Shi, Y. Zhu, Journal of Materials Chemistry A 1 (2013) 14766-14772.

672   [66] F. Dong, Z.W. Zhao, T. Xiong, Z.L. Ni, W.D. Zhang, Y.J. Sun, W.K. Ho, ACS Applied

673   Materials Interfaces 5 (2013) 11392-11401.

674   [67] H.J. Li, B.W. Sun, L. Sui, D.J. Qian, M. Chen, Physical Chemistry Chemical Physics 17

675   (2015) 3309-3315.

676   [68] J. Zhang, F. Huang, Applied Surface Science 358 (2015) 287-295.

677   [69] L. Shi, L. Yang, W. Zhou, Y. Liu, L. Yin, X. Hai, H. Song, J. Ye, Small 14 (2018) 1703142.

678   [70] J.X. Huang, D.G. Li, R.B. Li, Q.X. Zhang, T.S. Chen, H.J. Liu, Y. Liu, W.Y. Lv, G.G. Liu,

679   Chemical Engineering Journal 374 (2019) 242-253.

680   [71] P. Deng, H. Li, Z. Wang, Y. Hou, Applied Surface Science 504 (2020) 144454.

681 [72] F. Cheng, J. Yan, C. Zhou, B. Chen, P. Li, Z. Chen, X. Dong, Journal of Colloid Interface
682 Science 468 (2016) 103-109.

683 [73]A. Sánchez-Sánchez, F. Suárez-García, A. Martínez-Alonso, J.M.D. Tascón, Carbon 70 (2014)
684 119-129.

685 [74] G. Wang, Y. Zhao, H. Ma, C. Zhang, X.Dong, X. Zhang. Science of The Total Environment
686 756 (2020) 144139.

687 [75] R. Wang, X. Zhang, F. Li, D. Cao, M. Pu, D. Han, J. Yang, X. Xiang, Journal of Energy
688 Chemistry 27 (2018) 343-350.

689 [76] S. Zhao, X. Zhao, S. Ouyang, Y. Zhu, Catalysis Science & Technology 8 (2018) 1686-1695.

690 [77] D. Tsukamoto, A. Shiro, Y. Shiraishi, Y. Sugano, S. Ichikawa, S. Tanaka, T. Hirai, ACS
691 Catalysis 2 (2012) 599-603.

692 [78] Y. Shiraishi, S. Kanazawa, Y. Kofuji, H. Sakamoto, S. Ichikawa, S. Tanaka, T. Hirai,
693 Angewandte Chemie International Edition 53 (2014) 13454-13459.

694 [79]J.L. Yuan, X. Liu, Y.H. Tang, Y.X. Zeng, L.L. Wang, S.Q. Zhang, T. Cai, Y.T. Liu, S.L. Luo, Y.
695 Pei, C.B. Liu, Applied Catalysis B-Environmental 237 (2018) 24-31.

696 [80] G. Zuo, S. Liu, L. Wang, H. Song, P. Zong, W. Hou, B. Li, Z. Guo, X. Meng, Y. Du, T. Wang,
697 V.A.L. Roy, Catalysis Communications 123 (2019) 69-72.

698 [81] Y. Kofuji, S. Ohkita, Y. Shiraishi, H. Sakamoto, S. Tanaka, S. Ichikawa, T. Hirai, ACS
699 Catalysis 6 (2016) 7021-7029.

700 [82] Z. Zhu, H. Pan, M. Murugananthan, J. Gong, Y. Zhang, Applied Catalysis B-Environmental
701 232 (2018) 19-25.

702 [83] S. Zhao, X. Zhao, H. Zhang, J. Li, Y. Zhu, Nano Energy 35 (2017) 405-414.

703 [84] Y. Yang, Z. Zeng, G. Zeng, D. Huang, R. Xiao, C. Zhang, C. Zhou, W. Xiong, W. Wang, M.
704 Cheng, W. Xue, H. Guo, X. Tang, D. He, Applied Catalysis B: Environmental 258 (2019)
705 117956.

706 [85] Z. Wei, M. Liu, Z. Zhang, W. Yao, H. Tan, Y. Zhu, Energy & Environmental Science 11
707 (2018) 2581-2589.

708 [86] G.-h. Moon, M. Fujitsuka, S. Kim, T. Majima, X. Wang, W. Choi, ACS Catalysis 7 (2017)
709 2886-2895.

710   [87] S. Zhao, T. Guo, X. Li, T. Xu, B. Yang, X. Zhao, Applied Catalysis B-Environmental 224

711   (2018) 725-732.

712   [88] X. Li, J. Zhang, F. Zhou, H. Zhang, J. Bai, Y. Wang, H. Wang, Chinese Journal of Catalysis

713   39 (2018) 1090-1098.

714   [89] S. Li, G. Dong, R. Hailili, L. Yang, Y. Li, F. Wang, Y. Zeng, C. Wang, Applied Catalysis

715   B-Environmental 190 (2016) 26-35.

716   [90] J. Goclon, K. Winkler, Applied Surface Science 462 (2018) 134-141.

717